

Source Location and Dataset Incompleteness in Acoustic Emissions from Ice Tank Tests on Ice-Rubble-Ice Friction

Katerina Stavrianaki^{1,2}, Mark Shortt¹ and Peter Sammonds¹

¹*Institute for Risk and Disaster Reduction, University College London, London, UK*

²*Department of Statistical Science, University College London, London, UK*

Abstract

Experiments in rock mechanics conducted in the laboratory have revealed that the generation of elastic waves during micro-fracturing provide a small-scale analogue to seismogenic processes. These elastic waves are called acoustic emissions (AE). In contrast to rock, the seismic behaviour of ice under applied stresses is relatively unstudied and a robust statistical categorisation of acoustic events has not yet been performed. In analogy with experiments from rock mechanics, where it has been proven that statistical laws of seismicity are obeyed in AE events, we aim to characterise seismic activity in ice. This was done by measuring acoustic emissions during ice-rubble-ice friction tests conducted at the HSVA ice tank. Specifically, we studied AE data from two tests which used different rubble geometries: large round and small angular. Using these datasets from we first conduct source location of the AE activity. Secondly, we investigate the possibility of incompleteness in the AE datasets during periods of increased activity. Our results from source location show that the round rubble geometry gave higher acoustic activity at the sliding interfaces. We observe potential incompleteness in both datasets. This analysis has applications in field of seismology as well as in ice mechanics.

1. Introduction

Seismology is the study of the generation, propagation, and recording of elastic waves in the Earth (and other celestial bodies) and of the sources that produce them (Lay and Wallace, 1995).

On Earth's scale, a portion of the energy that is released during frictional sliding along faults is converted to seismic waves that propagate outwards. On a laboratory scale, when microfractures occur they generate elastic waves similar to those generated by earthquakes (Scholz, 1968). These waves are called acoustic emissions (AE). There are many similarities between earthquakes and AE events. Statistical laws that describe seismicity such as the Gutenberg-Richter and the Omori law are obeyed in AE events measured in laboratory samples of rock (Mogi, 1963; Scholz, 1968; Sammonds et al., 1992; Lockner, 1993) and therefore AE provides a great tool to study the seismogenic process.

AE originates from strain localisation and deformation (e.g. crack nucleation/dislocation) in a material, where a portion of the locally accumulated energy is released in the form of the transient acoustic waves. Measurement of AE is common in experiments on rock mechanics, and provides an in-situ insight into the state of damage of a sample subjected to a given strain. Whilst AE measurements are less common in ice mechanics experiments, there are still a number of studies on AE obtained from a number of different types of mechanical tests on ice. The majority of these studies have taken place in the laboratory (e.g. Gold, 1960; St Lawrence and Cole, 1982; Sinha 1982, 1985; Rist and Murrell, 1994; Weiss and Grasso, 1997; Cole and Dempsey, 2006; Li and Du, 2016) where conditions are controlled and ambient noise is typically low. However there have also been several (but fewer) studies documenting AE recorded from experiments on sea ice performed in-situ in the field (e.g. Langley, 1988; Xie and Farmer, 1994; Langhorne and Haskell, 1996; Cole and Dempsey, 2004; Lishman et al., 2019a, 2019b). Recently, Marchenko et al. (2019) and Lishman et al. (2019a) have also documented results from AE ice tank experiments.

A common trend in AE research on ice, particularly in earlier studies, is the focus on obtaining the temporal variation in AE activity, and its correlation with applied load. From this, potential source mechanisms can be inferred. In general, two primary source mechanisms have been identified for ice: dislocation breakaway and microcracking. Dislocation breakaway has been documented as a potential source mechanism in creep tests on ice under compressive loading (St Lawrence and Cole, 1982, Weiss and Grasso, 1997) and cyclic loading of cantilever beams (Langhorne and Haskell, 1996). Furthermore, Weiss and Grasso (1997) recorded AE in the laboratory during creep deformation of single crystals of ice under uniaxial compression and torsion creep, and concluded that creep is a marginally stable state rather than a steady-state.

Microcracking is commonly identified in AE from tests involving ice fracture (Sinha, 1982; Rist and Murrell, 1994; Cole and Dempsey, 2004, 2006; Li and Du, 2016; Lishman et al., 2019b) but has also been suggested to occur in creep tests when the stress level is high (St Lawrence and Cole, 1982). Recently, Li and Du (2016) measured AE in the laboratory tests on fresh ice samples subjected to uniaxial compression and three-point bending. Analysing the waveforms of the individual AE signals, and plotting the average frequency against the rise amplitude, they were able to differentiate between tensile and shear cracking events. They found that shear cracking was the primary failure mode for ice under compression, whereas bending failure was controlled by tensile movement cracks. Lishman et al. (2019a) used the

same analysis on AE data obtained during field tests on sea ice under compression, tension, shear and indentation, but were unable to verify the results of Li and Du (2016), probably due to the 100 kHz low frequency cut-off of the instrumentation, which meant lower frequency shear cracks could not be recorded.

There exists a number of AE analyses used in rock mechanics and seismology that have yet to be conducted on ice. In this paper, we aim to implement two such analyses: 1) source location of AE events, and 2) short term aftershock incompleteness (STAI) of the AE datasets. We use AE data obtained from friction tests on saline ice conducted at Hamburgische Schiffbau-Versuchsanstalt (HSVA) in 2017. In these tests, numerous types of ice rubble was introduced between sliding interfaces with the aim of investigating the influence of fault gouge on the frictional behaviour.

To our knowledge, no previous studies on AE generated during ice-ice friction tests have been conducted, but we may postulate that in the static regime, the shear fracture of freeze-bonds is a probable source mechanism. This is particularly true in the case of a floating ice sheet, where surrounding water will act to amplify the bonding process. We can also make analogies with results from rock mechanics to gain an insight into other potential source mechanisms. From data obtained from double-shear experiments on rock, Sammonds and Ohnaka (1998) suggest that the maximum AE rate coinciding with the maximum shear stress is a result of fracturing asperities at the fault surfaces. As the fault slides, a fractal length distribution of cracks grows as contacting asperities interact. Other studies (Michlmayr et al., 2012; Jiang et al., 2017) also suggest the breaking of asperities between solid surfaces as a potential source mechanism of AE generated during shearing of geological materials.

In the presence of a fault gouge within the sliding interface (analogous to the rubble region in our experiment), it is suggested by Michlmayr et al. (2012) that acoustic signals may be generated by the failure of buckling force chains and frictional slip between grains. Furthermore, it is noted by Mair et al. (2007) that the contact area between grains within the gouge is an important factor in determining the average AE occurrence rate.

If we wish to assess the evolution of damage in ice subjected to mechanical loading, it is desirable to map these deformation events so we may predict where or how the ice will fail. In rock mechanics this is done via source location (e.g. Brantut, 2018). Although there are several methods of source location, the basic concept is the same - arrange an array of sensors across the surface area of the material to 'triangulate' the events given measurements of wave speed and arrival times.

For investigation of STAI, we introduce the Gutenberg-Richter (G-R) law (Ishimoto and Iida, 1939; Gutenberg and Richter, 1944) which gives the exponential relation between the frequency of earthquakes (N) and their magnitude (M) in a given region and period of time. This law is described mathematically as follows:

$$\log_{10}[N(m)] = \alpha - b(m - m_t) \quad (1)$$

In the equation above $N(m)$ is the number of earthquakes with magnitude greater than or equal to m_t α and b also known as the b -value are the ordinate intercept and slope, respectively, of the line that relates m_t and $\log_{10}N(m)$.

The G-R law corresponds to a power law in terms of the energies which is a typical sign of scale-invariance (Main, 1996; Turcotte, 1997) and it has been shown to hold for magnitudes as small as -4.4 (Kwiatek et al., 2010). The b-value is also linked with the magnitude of completeness of an earthquake catalogue. The magnitude of completeness (M_c) is the magnitude above which we are certain we have a complete dataset, and this is particularly important for any statistical analysis.

Here we use the equation from Sammonds and Ohnaka (1998) that relates the logarithm of AE hit frequency with the amplitudes. The amplitudes are measured in dB and divided by 20. This reproduces a G-R law for our experimental data and we can find the corresponding b-value. The b-value and its variations during a laboratory experiment is frequently used to monitor the fracturing process inside specimen both for rock deformation (e.g. Mogi, 1963; Scholz, 1968; Lockner, 1993; Sammonds and Ohnaka, 1998) but also in ice.

Recent studies (Li and Du, 2016; Lishman et al., 2019a, 2019b) have applied the concept of b-value to AE data from ice mechanics experiments. They calculated the temporal change in the b-value with the aim of inferring the evolution of damage within the material. Li and Du (2016) calculated this temporal change for laboratory tests on compression and three-point bending, and found that for both test types, the b-value gradually increased to above 1 as loading was applied, indicating that microcracks developed stability. During and after failure, the b-values dropped sharply, indicating a rapid expansion of cracks. From AE data obtained from compression and indentation tests on sea ice conducted in the field, Lishman (2019b) found respective b-values of 1.80 and 1.59. The temporal variation in b-value was also investigated for both types of tests investigated the temporal change in b-value for field tests. They found that as the ice evolved towards failure, the b-value decreases and tends towards 1. In the case of compression, the b-value increased again during unloading. Furthermore, Lishman et al. (2019a) deduced the temporal change in b-value from AE data obtained in the HSVA Ice Tank from wave-induced deformation of a floating saline ice sheet, and speculated that cracks may have formed and healed repeatedly under cyclic motion. In each of the aforementioned studies, it is noted that analysis of b-values can provide a useful tool in predicting failure in ice under deformation.

STAI is a phenomenon observed in earthquake data. For a short period after large earthquakes the seismic activity is increased (we have aftershocks), and during this period smaller earthquakes can be lost in the coda of the larger events. The missingness of the small data has an effect on the b-value during this period. Since the b-value describes the ratio between large and small earthquakes, the lack of small events will cause an artificial decrease in the b-value.

Borrowing from seismology, we aim to look at these periods of increased activity and determine if we observe incompleteness. We use the method developed by Hainzl (2016), to find incompleteness. In his paper Hainzl demonstrates how the magnitude of completeness varies with seismicity rate. The b-value is estimated using a maximum likelihood method for different seismicity rates. Incomplete recordings will produce an apparent decrease in the b-value since we assume a constant frequency – magnitude distribution the data.

2. Experimental Set-up

AE data was gathered from a series of slide-hold-slide friction tests on saline ice conducted at the HSVA Large Ice Model Basin (LIMB) with the aim of investigating the influence of ice

rubble gouge in between the contacting interfaces. A full description of the friction tests can be found in Scourfield (2019).

The HSVA LIMB measures 78m x 12m x 2.5m and contains NaCl-doped water to a salinity of 6.8 ppt. The structure of S2-type columnar ice was replicated using ‘artificial full scale ice’. The air temperature was set to -8°C for the duration of the tests and the average initial ice thickness (at the start of the experimental preparation) was 22cm and had reached 29cm by the end of the tests. The saline ice had bulk salinity of around 1.5 ppt and a bulk density of 919 kg/m^3 .

The experimental set-up is shown in Figure 1a. The experiment utilised a double-direct-shear configuration, comprising a central ice block measuring 3.5m x 1.5m and a side ice beam either side, both measuring 1.5m x 0.8m. The central block and the side beams were separated by a 0.5m wide open channel of water containing rubble blocks, which were varied in size and shape over the experiment. A nominal normal load of 1.5kN was applied on each side beam by a set of side load frames. The central block was pushed under the normal load using a pusher plate attached to the moveable main carriage. The rate- and state-dependencies were investigated by varying the sliding velocity and hold time respectively.

Nine AE transducers were deployed on the central ice block by making 1 cm deep holes and then freezing using fresh water. The spatial arrangement of the AE transducers on the central block is shown in Figure 1b. The transducers comprised PZT-5h compressional piezoelectric crystals measuring 15mm in diameter and 5mm in thickness, with a 500 kHz central frequency. These crystals were soldered onto copper discs and potted in epoxy. The signals from each transducer were amplified locally by 40dB via Vallen preamplifiers. Figure 2 shows an AE transducer connected to a Vallen preamplifier. The amplified signals were then transmitted to a Vallen AMSY5 system, which recorded a hit (maximum amplitude and time) if the signal exceeded a threshold of 40dB. For each registered hit, the Vallen system also records a $400\ \mu\text{s}$ transient waveform (voltage vs time) beginning $50\ \mu\text{s}$ prior to the triggering of the threshold. Sampling frequency of the transient is 5MHz. Observations of the shape of these transients are useful in noise filtering, which is discussed in the next section.

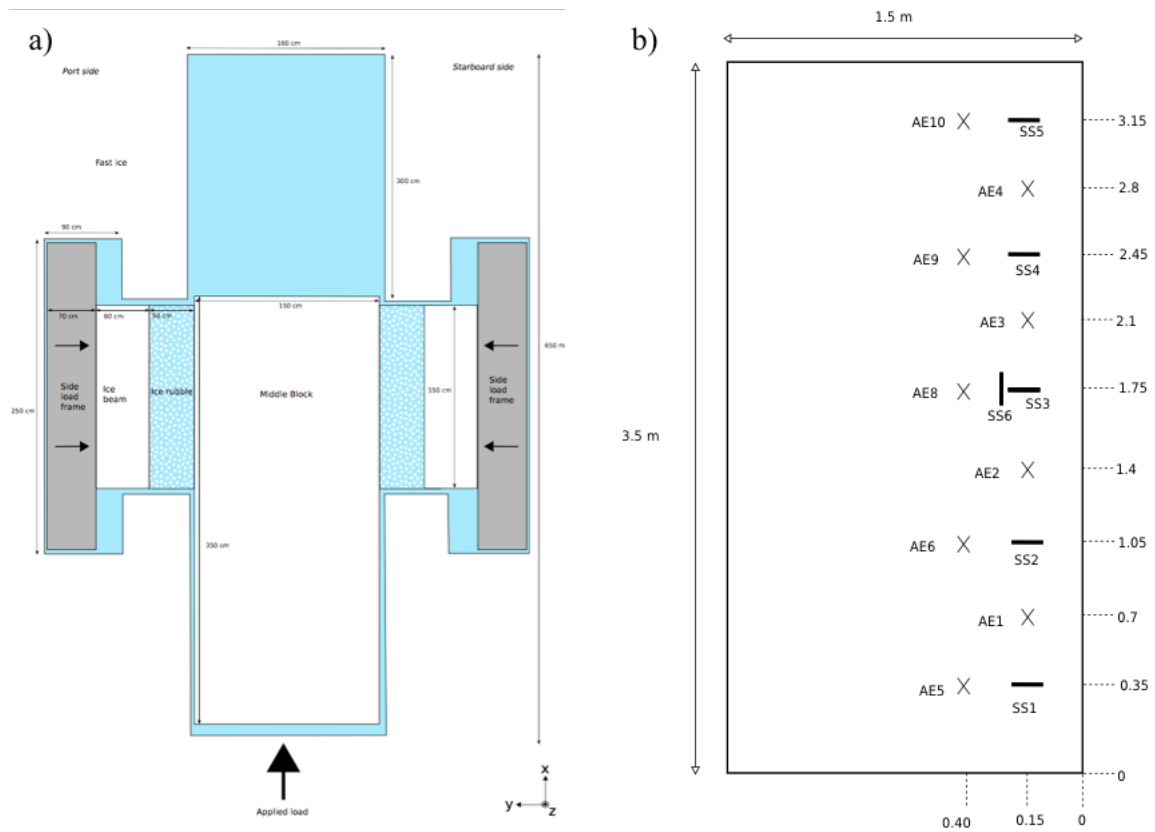


Figure 1: a) overall experimental set-up for the friction tests, and b) location of instruments on the central ice block – AE transducers are shown as crosses, mercury stress sensors (SS) are also shown (Scourfield, 2019)



Figure 2: Example of an AE transducer and Vallen pre-amplifier used in the friction tests

For the analysis in this paper, we use AE data from two selected tests, chosen on the basis of a clear spike in coefficient of friction under the initiation of motion of the central block. These tests were named ‘Test 6b1’ and ‘Test 9b’ respectively and conveniently shared the same hold time and sliding velocity, but two different types of rubble – with varying size and shape. This, enabled a direct investigation into the influence of rubble type on the acoustic activity. A

summary of the properties of each test is given in Table 1. Plots of coefficient of friction against time for each test are given in Figure 3.

Table 1: Summary of test properties for Test 6b1 and Test 9b

	Test 6b1	Test 9b
Rubble Type	Large round	Small angular
Rubble Dimensions	16.5 cm diameter, 9 cm depth	10 cm short axis, 17 cm long axis, 9 cm depth
Nominal Normal Load	1.5kN	1.5kN
Hold Time	10,000 s	10,000 s
Nominal Sliding Velocity	0.3 cm/s	0.3 cm/s
Sliding Distance	20 cm	20 cm

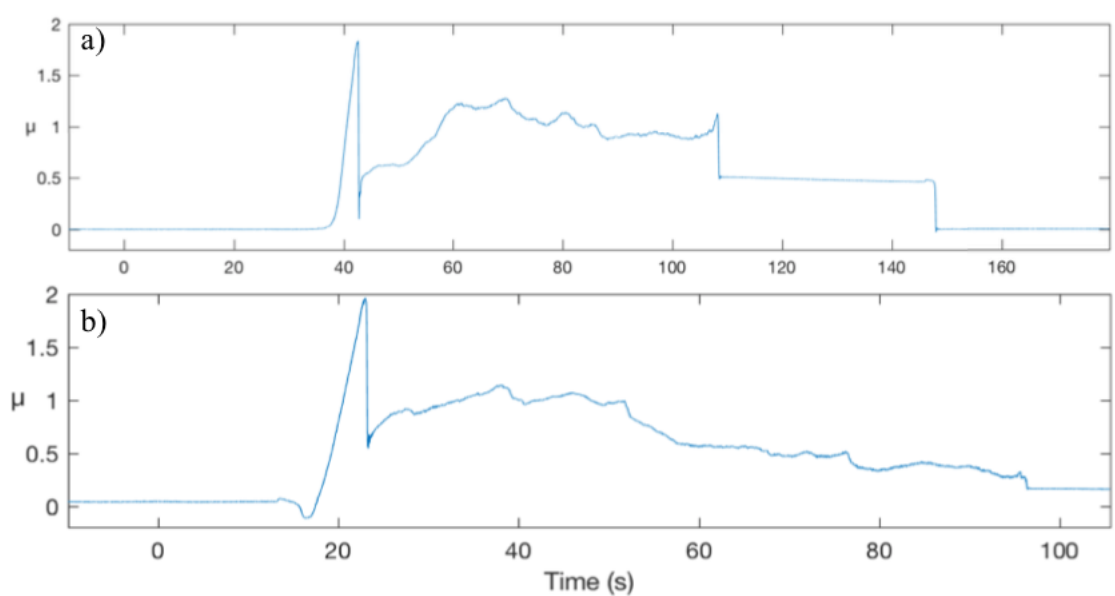


Fig 3: Plots μ vs time for a) Test 6b1, and b) Test 9b. Clear spikes in coefficient of friction are visible at the initiation of sliding (adapted from Scourfield (2019))

In both tests there are clear spikes in the coefficient of friction at the initiation of sliding, corresponding to the static value and can be physically interpreted as the breaking of freeze-bonds developed between the ice blocks and the rubble during the hold period. Following this spike, the value of μ drops sharply to a relatively steady state corresponding to dynamic friction. The clear distinction between the static and dynamic friction regimes in these tests aids with the interpretation of the acoustic data. It should be noted that other tests conducted did not exhibit such a clear distinction.

3. AE Datasets and Noise Filtering

The data acquisition period ran before and after the actual start and end time of the tests. Table 2 shows characteristics of the AE data from each test. In total there were 54165 hits recorded in Test 6b1, and 70471 hits recorded in Test 9b. The raw data from each test are given in the top two panels of Figure 4. It can be seen that in both tests there is a large amount of noise, which needed to be filtered before any analysis could be performed. It is possible that this noise originated at the hardware level due to the inherent noise floor of the instrument chain and is

thought to be of similar magnitude to the test source. Both the test signal and the noise floor were then subject to 40 dB gain provided locally by the Vallen preamplifiers.

Removal of noise was done in post-processing based on two criteria. The first criterion was time – the start and end times of the test, which were easily identified by viewing the overall AE activity. Any events occurring before or after these times were removed. The remaining events were then filtered based on a frequency criterion, similar to Lishman et al (2019) and Marchenko et al. (2019). The frequency spectrum of a given hit is deduced by taking a fast Fourier transform of the transient waveform data. From this, the frequency at the maximum amplitude of the spectrum (FMXA) is calculated for each hit. By plotting FMXA vs time, it is possible to deduce frequency bands of noise, which occur throughout the duration of the logging, irrespective of the test start and end times.

Table 2: Characteristics of AE data from Test 6b1 and Test 9b

	Test 6b1	Test 9b
Total Hits	54165	70471
Test Start Time t_{start}	43.5 s	76.9 s
Test End Time t_{end}	139.5 s	159.0 s
Hits After Filtering	5231	3325

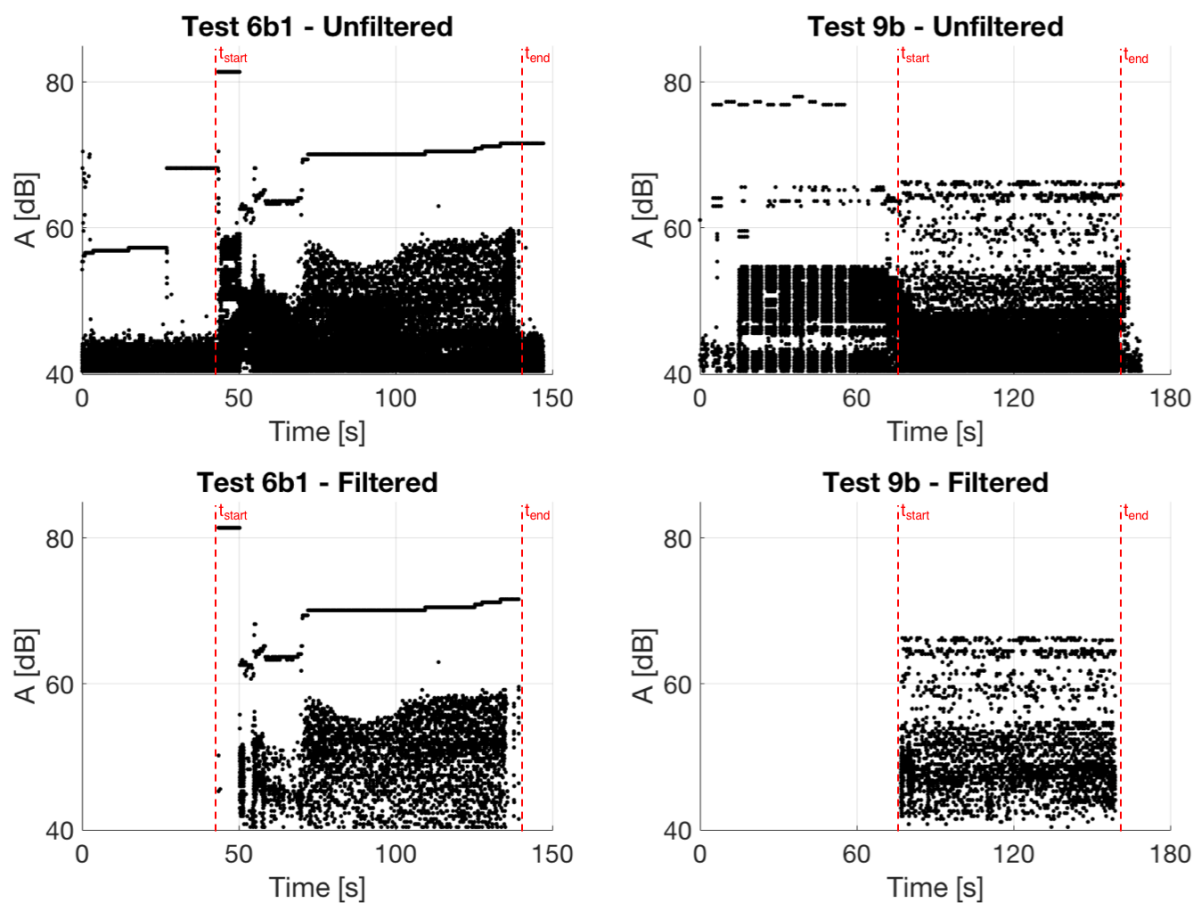


Figure 4: Unfiltered and filtered datasets of maximum hit amplitude (A) with time for Test 6b1 and Test 9b. The start and end times of both tests are also identified.

The FMXA vs time data for both tests are plotted in the top panels of Figure 5 for all hits. Focusing first on Test 6b1, it can be seen that a large number of hits occur across a narrow frequency band, between 420-450 kHz. Events within this frequency band occur across the duration of the logging period, and thus can be identified as noise. Now focusing on Test 9b, it can be seen that the noise is not confined to one frequency band and exists superimposed on real data. Therefore, to distinguish between the two we conducted further filtering based on analysis of hit duration (D) and counts (CNTS), which is the number of times a waveform crosses the threshold. Figure 6 gives a graphical description of these two variables. We conducted this filtering over the frequency band $100 < F < 200$ kHz which appeared to show a high hit activity with noise superimposed. We found that the hits in this frequency region broadly fell into two regimes for D and CNTS. These corresponded to 1.) $D < 10 \mu\text{s}$, $\text{CNTS} = 1$ and 2.) $D > 10 \mu\text{s}$, $\text{CNTS} \neq 1$

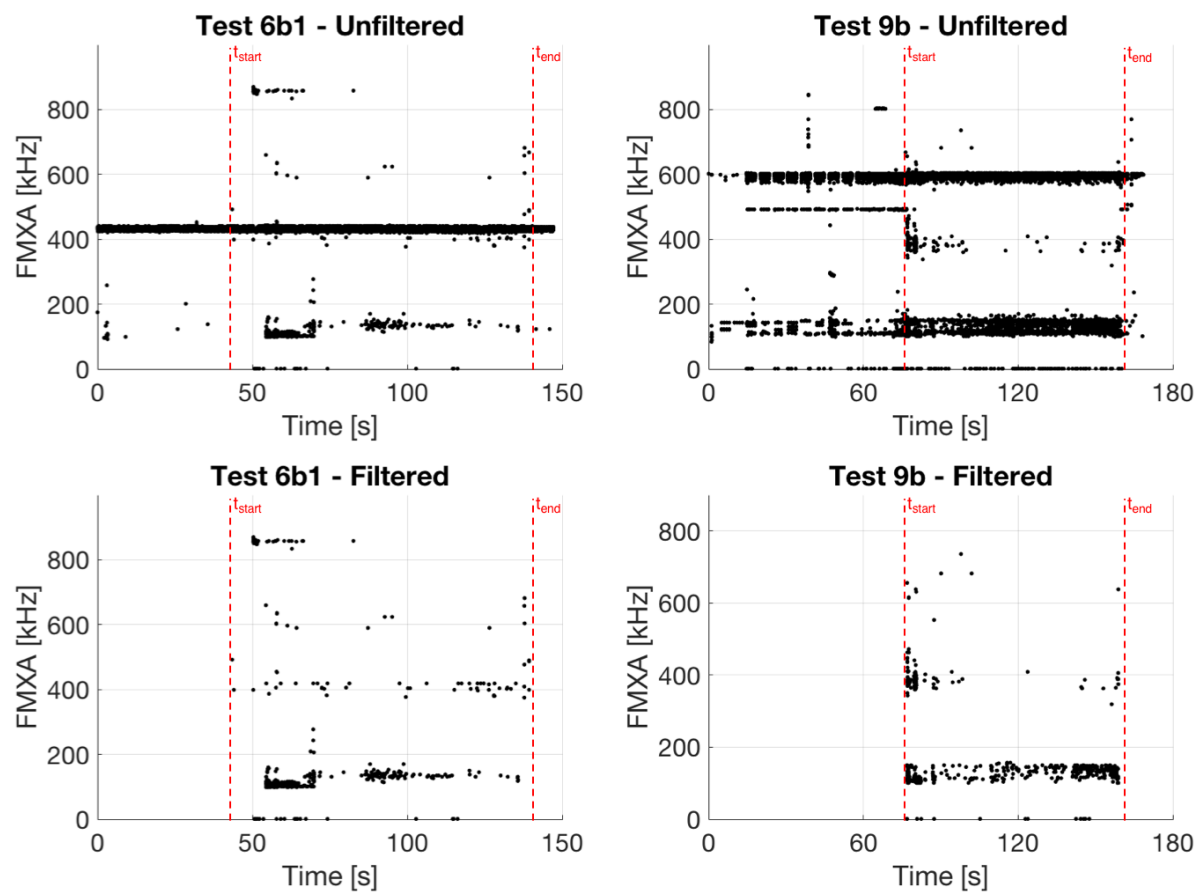


Figure 5: Unfiltered and filtered datasets of frequency at maximum hit amplitude (FMXA) with time for Test 6b1 and Test 9b. The start and end times of both tests are also identified.

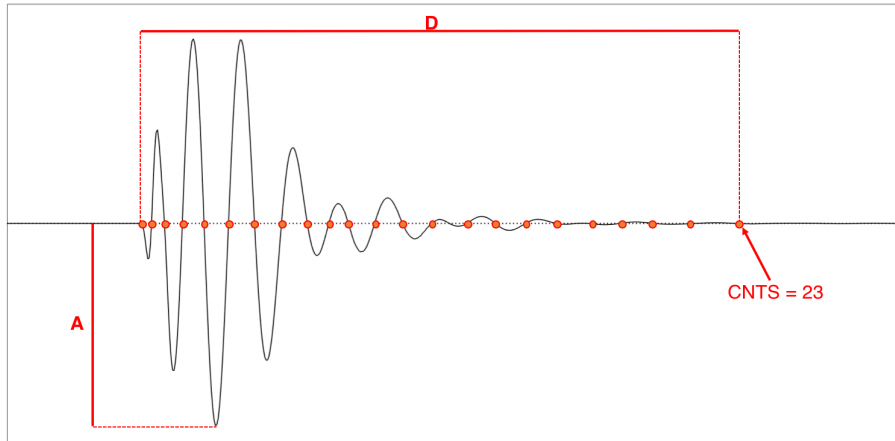


Figure 6: Typical transient waveform recorded for an individual hit. The maximum amplitude (A), hit duration (D) and counts (CNTS) are also labelled.

Figure 7 shows the hits filtered on these regimes. It can be seen in the latter criteria ($D > 10 \mu\text{s}$, $\text{CNTS} \neq 1$), there exists concentrations of hits in two bands which are consistent with noise existing outside the test period. Therefore, we believe these criteria to be sufficient for filtering over this frequency region. The filtered data for amplitude and FMXA are given in the bottom panels of Figures 4 and 5 respectively. The filtering gave less than 10% hits remaining from the total.

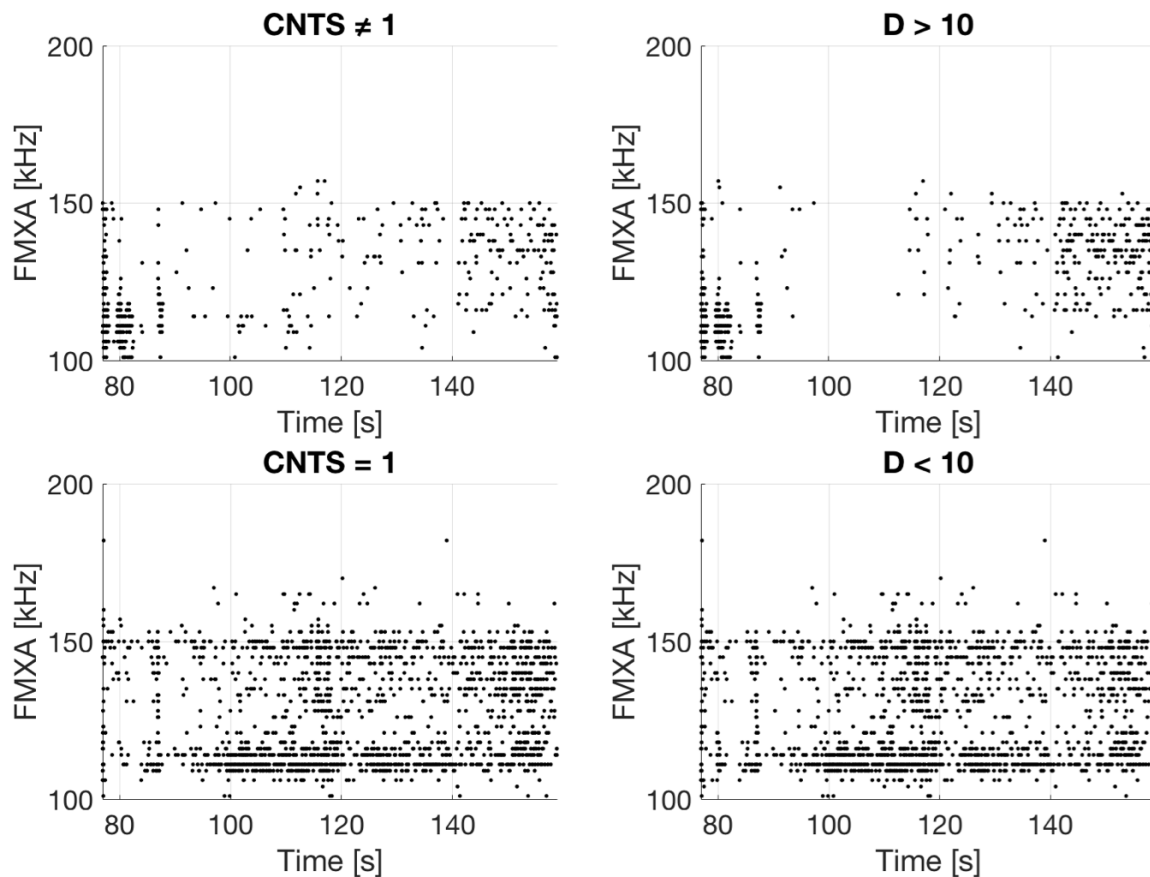


Figure 7: Filtering of AE hits for Test 6b1 in the frequency range 100-200 kHz. We filter this data based on two regimes for D and CNTS: 1.) $D < 10 \mu\text{s}$, $\text{CNTS} = 1$ and 2.) $D > 10 \mu\text{s}$, $\text{CNTS} \neq 1$. We believe that the latter conditions correspond to noise

4. AE Source Location

The Vallen acquisition system measures the transient waveforms of each hit, and from this and due to the fact that we use multiple transducers over the area of the ice sheet we can obtain basic source location of microseismic events.

The waveform data from filtered hits on each channel were grouped into individual AE structures. Each structure (known as an AE event hereafter) contained a single hit from each channel, which were chosen on the basis similar hit times. Thus, it is assumed that each selected hit in a given AE event corresponds to an individual deformation event, received at different times for each transducer. It should be noted that prior to the generation of these AE event structures, the number of filtered hits on each channel was determined. Any channels with a comparatively small number of filtered hits were disabled from this analysis. For Test 6b1, channels 4 and 10 were disabled, whilst for Test 9b channels 4, 9 and 10 were disabled. It should also be noted that channel 7 was unused in all tests.

To conduct source location, it was necessary to obtain the p-wave velocity through the ice. This was done using the calibration function on the Vallen system, which emits four evenly spaced pulses (1 per second) on each channel consecutively. The frequency of the emitted pulses was approximately 150 kHz. These pulses are received by surrounding channels at a lower amplitude a short time Δt after the emission pulse. A typical hits vs time graph for such a calibration test is shown in Figure 8. Knowing the distance d between the emitting and receiving transducers it is possible to obtain an estimate for the p-wave velocity v_p via the basic distance-time relation:

$$v_p = \frac{d}{\Delta t} \quad (4)$$

This calculation was conducted for each emitted hit with an obvious corresponding detected hit. The average velocity was then calculated over all emitted-received pairs and was found to be $v_p=3213$ m/s. Our value of v_p is slightly higher than those measured in field sea ice [Xie and Famer (1994), Marchenko et al. (2020)], but is slower than in freshwater bubble-free ice [Vogt et al. (2008)]. We believe that our intermediate value for v_p is a result of the low water salinity used in the tank. It can be possible for the underlying water to have an influence on the wave velocity, resulting in an artificial decrease in the measured value. Since our value for v_p lies within the range of previously measured values, and since the ice was relatively thick, we do not believe that water had a significant influence in our study.

It should be noted that for a complete analysis of source location, the degree of anisotropy of p-wave velocity should be determined by deploying transducers in all directions across the area and depth of the ice block. However, in this analysis, we use an isotropic velocity model, since the position of the transducers meant we could only determine p-wave velocity in two directions.

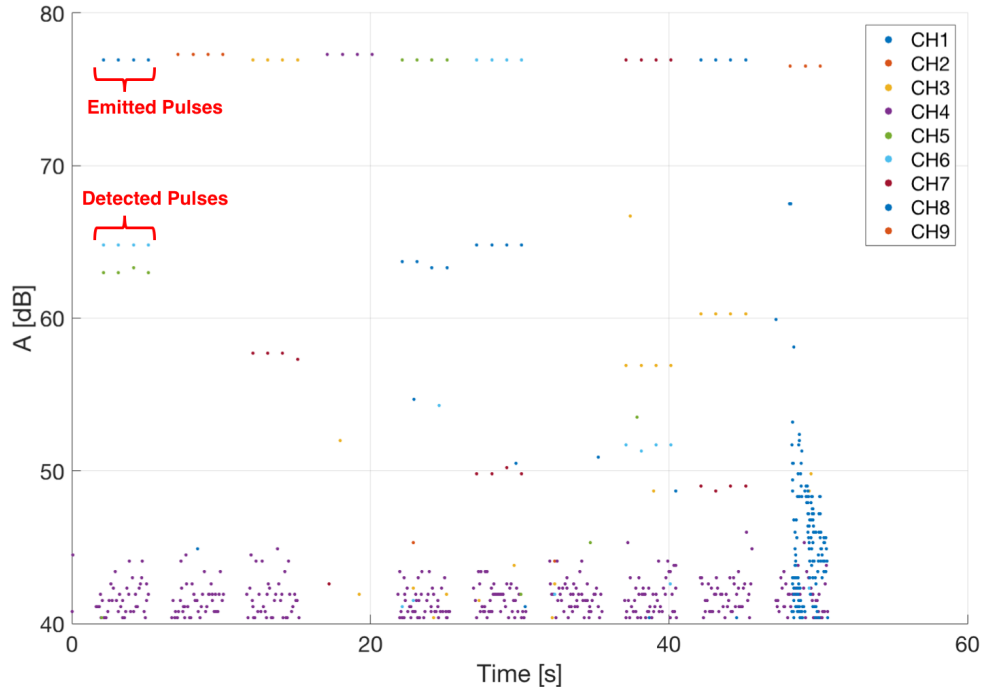


Figure 8 Typical hits vs time graph for a calibration run, which we use to identify the p-wave velocity. Four evenly spaced pulses are emitted by each channel consecutively. These pulses are detected on surrounding channels.

The next step was to determine the p-wave arrival times at each transducer. This was done via the RMS amplitude method, which calculates an autopicking function via a moving window approach (ASC, 2014). At each waveform datapoint i , two windows are generated – a front window of length (in datapoints) NF and a back window of length NB . The value of the autopicking function is given by Equation (3), and represents the difference in energy contained in the front window compared with the back window:

$$F_i = \frac{\sum_{j=i+1}^{i+NF} A_j^2}{\sum_{j=i-1}^{i-NB} A_j^2} \quad (3)$$

Where A_j is the amplitude. This gives an array of RMS values of the length of datapoints within the waveform. We use the following values: $NF=100$, $NB=150$, which were deduced by viewing transient waveforms. The p-wave arrival time was then deduced by calculating the time in the waveform that coincides with the maximum value of RMS. Each event then has an arrival time for each channel and given these arrival times, in addition to the p-wave velocity and the relative positions of the transducers, an estimate for the source location of a given event can be obtained. Events identified from Test 6b1 and Test 9b are plotted onto the central ice block geometry (see Figure 9) in Figures 10a and 10b respectively. It should be noted that, since the transducers were all positioned at the same depth within the central block, we can only estimate source location across a plane at this depth. Incorporation of depth effects requires positioning of transducers throughout the thickness of the ice block.

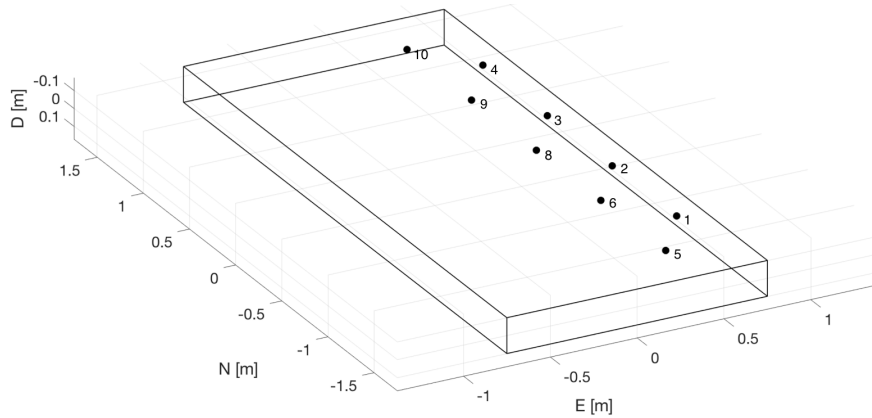


Figure 9: Geometry for source location corresponding to the dimensions of the central ice block. The positions of the AE transducers are also shown

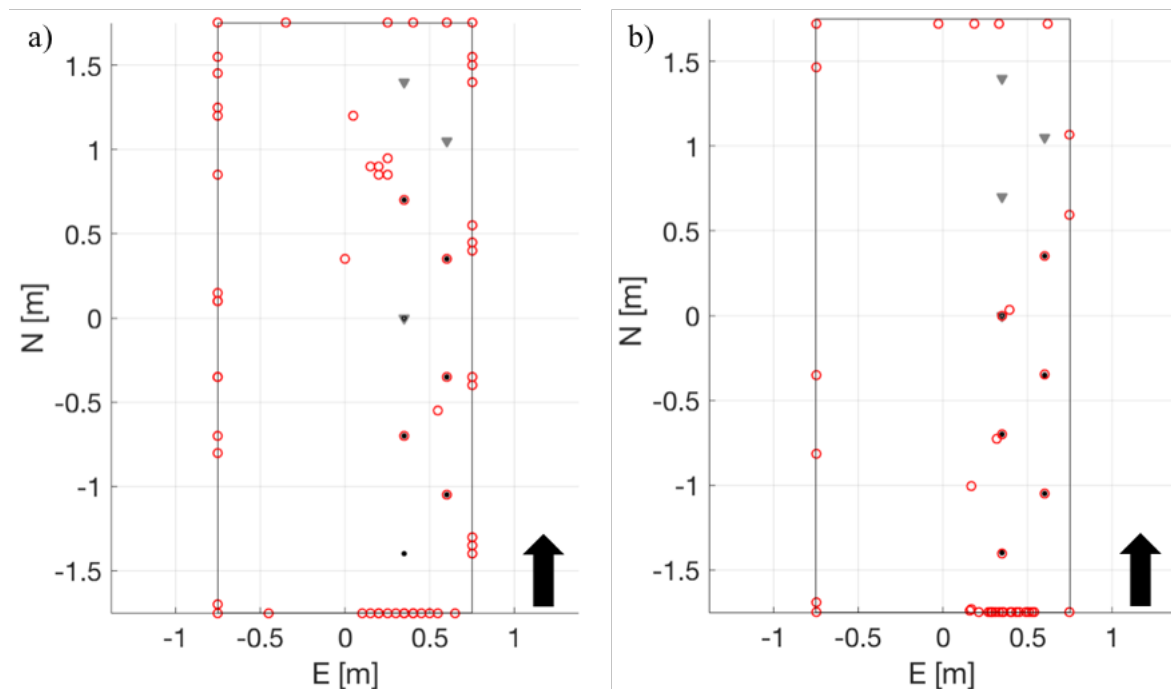


Figure 10 – Results from source location for a) Test 6b1 and b) Test 9b plotted on the geometry of the central ice block, The black arrows represent the direction in which the pushing load was applied. The triangles represent channels which were disabled from the analysis

For Test 6b1, a total of 4967 AE events were identified, which was reduced to 331 events after filtering. For Test 9b, a total of 6674 AE events were identified, which reduced to just 67 events after filtering. Thus there were relatively fewer AE events in Test 9b, which is reflective of the high amount of noise recorded during this test.

Overall, there were more events located at the sliding edges in Test 6b1, and thus we may conclude that large round rubble gave higher AE activity than the small angular rubble. This may be due to the different geometries in the two types of rubble. Theoretically, each piece of round rubble should only create a single point of contact with the central ice block (and other

rubble pieces), whereas in the angular rubble it is possible for an entire face to contact and even tessellate with one another.

Acoustic activity at the interacting edges may be initially governed by freeze-bonding between the ice rubble and the central ice block forming during the previous 10,000 s hold period. We can thus assume that greater AE activity in the round rubble resulted (at least initially) from a greater number of individual freeze-bond failure events. At the initiation of sliding, it may have been easier for bonds in round rubble to break since in this geometry both rotational and linear forces will be acting in significant proportions. In the case of the angular rubble, rotational forces should be less apparent. Transmission of force chains (as noted by Michlmayr et al. [2012]) is also easier with round rubble which may have further increased freeze-bond failures between individual blocks. Following initial freeze-bond failure, in the sliding regime, further AE may be generated from sliding between the central block and the (now freed) rubble pieces.

One interesting similarity between the two tests is the clustering of events at the near end of the ice block. We attribute this to indentation in the ice block caused by the pusher plate which was located at the same end. Indeed in Test 9b, where this clustering is particularly apparent, it was noted that there was audible creaking from the pusher plate due to the high load (7.7 kN) experienced at the point of static friction.

It is also interesting to note the events located away from the edges of the central ice block. Since the AE activity is expected to be confined to sliding edges, we do not believe that these events were generated by deforming ice. Rather, we believe that these events originated from other noise sources resulting from the motion of the central block, such as surrounding water that tended to flood the top surface, or the movement of wires that connected the instruments to the main carriage.

5. Statistical Analysis of Short Term Aftershock Incompleteness (STAI)

In this section of the paper we conduct an investigation into STAI in the AE datasets. To do this, we follow the methodology described in Hainzl (2016), adjusting the bin size to an appropriate value for our experiments. As a proxy for earthquake magnitude, we divide amplitude values by 20, as per Sammonds and Ohnaka (1998). This method estimates the b-value for filtered events with increasing event rate using the maximum likelihood method for event bins with at least 5 amplitudes using (Aki, 1965; Marzocchi and Sandri, 2003, Hainzl, 2016):

$$\hat{b} = \frac{1}{\ln(10) \langle m - (M_c - 0.5 \Delta m) \rangle} \quad (4)$$

Where: m is magnitude

$M_c = 2$ is the magnitude of completeness

Δm is binning interval, set to 0.01 as per the precision of recorded amplitudes

The magnitude of completeness is the magnitude above which we are certain we have complete recording of the data and is calculated by fitting the G-R Law to all the filtered data. It corresponds to the lowest magnitude to which the linear regime begins.

Figure 11 shows the G-R fitting for the AE data in both tests. Events were grouped by amplitude in bins of size 3dB. The b-value is obtained by taking the gradient of the linear

trendline, and was found to be $b=0.71$ for Test 6b1 and $b=0.89$ for Test 9b. We do not observe the non-linear regime existing at low magnitudes for earthquake data. In contrast to smaller scale experiments, where the G-R law is observed (e.g. Sammonds and Ohnaka, 1998) the fit in our dataset has a greater uncertainty. This could be due to an increase in uncertainty of all parameters involved in all the calculations due to the large scale nature of the experiment. The loose fit may also be a consequence of the heterogeneity of the source mechanisms, such as those reflecting breaking freeze-bonds compared with those generated during subsequent sliding. Due to the loose fit of the data, it is hard to obtain a precise b-value and the corresponding value for M_c . As a result, we take the $M_c=2$, corresponding to the minimum amplitude datapoint.

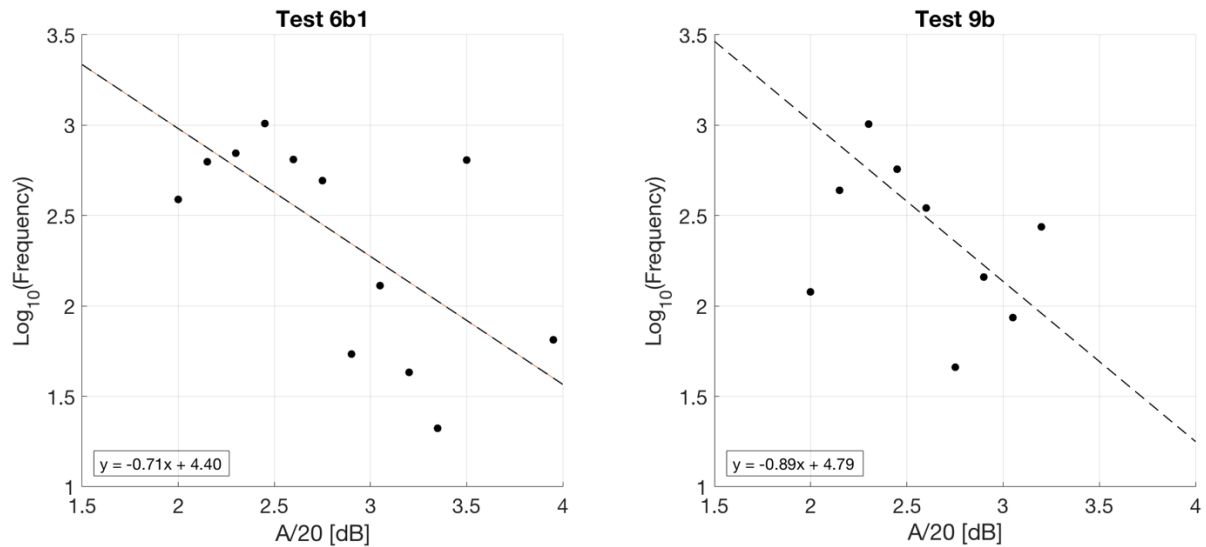


Figure 11: Log(frequency)-magnitude data for both tests. Amplitudes were binned in 3dB increments. Equations for G-R linear fittings are shown, which are used to determine b-values

Figure 12 shows the rate-varying b-value obtained from data in both tests, estimated from Equation 4, for rate bin-sizes between $10-1000 \text{ s}^{-1}$. These rate-bin sizes were deduced by observing the typical count rates occurring during our experiments, as well as those found in Marchenko et al. (2019), who measured AE data using the same apparatus described here. In both figures, there is a noticeable decrease in b-value, which may indicate incompleteness in the datasets, as per Hainzl (2016). Following this decrease, the b-value stays constant at around the values obtained in the Figure 11. The onset of decreasing b-value occurs at a rate 40 s^{-1} for Test 6b1 and 20 s^{-1} for Test 9b.

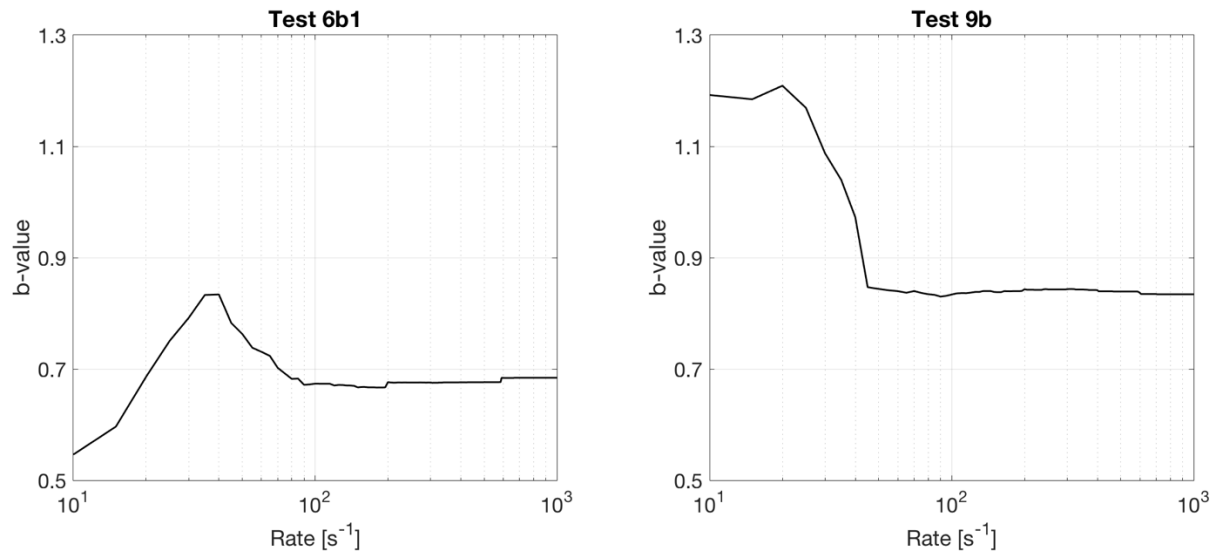


Figure 12: Plots of b-value against hit rate for Test 6b1 and Test 9b. Both tests exhibit at decrease in b-value, which may indicate incompleteness

The fact that we observe decreasing b-value in both tests indicates the potential for incompleteness in AE datasets in ice mechanics experiments. However, uncertainties in the calculations should be noted, particularly in the continuous calculation of b-value with rate from datasets which already give a loose fit to the G-R law. We aim to continue our investigation of incompleteness in AE datasets from other ice tank tests, as well as from concurrent smaller scale ice friction tests conducted in the UCL Ice Physics Laboratory. If incompleteness is a common feature in these datasets, it indicates that this would be an important phenomenon to consider in the analysis of any AE measurements in ice.

6. Conclusions

In this paper, we have presented two types of AE analysis from data obtained from ice-rubble-ice friction tests conducted at the HSPA LIMB. Specifically, we took data from two individual tests chosen on the basis of a clear spike in the value of μ at the initiation of sliding: Test 6b1 using large round rubble, and Test 9b using small angular rubble. This enabled a direct investigation into the influence of rubble geometry on the acoustic behaviour.

The AE data from both tests was filtered based on two criteria: 1) start and end times of the test, and 2) values for frequency at maximum amplitude (FMXA). For Test 6b1, further filtering based on hit duration and counts was conducted to eliminate noise in regions of high hit activity.

The spatial arrangement of AE transducers enabled source location of AE events to be conducted. P-wave velocity was deduced via calibration assuming an isotropic velocity model, with the averaged calculated to be $v_p=3213$ m/s. P-wave arrival times were calculated using an RMS amplitude method. We found a greater number of events to be located at the sliding ice edges in Test 6b1, which we attribute to the rubble geometry and its influence on the breaking of freeze-bonds developed during the previous 10,000s hold period.

The b -values were determined in both tests. We calculate $b=0.71$ and $b=0.89$ for Test6b1 and Test9b respectively, and in both cases the data is only a loose fit to the linear G-R Law, probably due to a combination of heterogeneity of the source processes and uncertainties

related with the large-scale nature of the experiments. Our b-values are low compared those calculated in Lishman et al. (2019a, 2019b) and indicate a comparatively high number of large events. We speculate that our lower values are a reflection of the different types of mechanical tests. In contrast to compression, indentation and flexure, where high levels of (small amplitude) microcracking are likely, in our experiment a significant proportion of recorded AE likely originated from larger-scale fracturing of freeze-bonds that formed between central block and the rubble in the previous 10,000s hold period.

Finally, we conducted an investigation of STAI in the AE datasets by calculating the b-value at rates between 10-1000 s⁻¹. In both tests we see a decrease in the b-value, which may indicate incompleteness in the datasets, as per Hainzl (2016). Following this decrease, the b-values remained constant at levels similar to that obtained over the entire filtered datasets. However, due to loose fitting of the AE data to the G-R Law, a degree of uncertainty exists in this analysis. In future, we aim to continue this investigation of STAI in further AE datasets from both ice tank tests and smaller scale laboratory tests.

Acknowledgements

The experiment described in this publication was supported by the European Community's Horizon 2020 Research and Innovation Programme through the grant to HYDRALAB-PLUS, Contract no. 654110. This project was led by Sally Scourfield, and we would like to thank her for permission to use this data. We would also like to thank the Hamburg Ship Model Basin (HSVA), especially the ice tank crew, for the hospitality, technical and scientific support and the professional execution of the test programme in the Research Infrastructure ARCTECLAB. Thanks to Ben Lishman for useful discussions and recommendations on both the experimental set-up and the analysis. Finally, thanks to Nic Brantut for providing the initial MATLAB code for AE source location.

References

- Aki, K. (1965), Maximum likelihood estimate of b in the formula $\log n = a - bm$ and its confidence limits, *Bulletin of the Earthquake Research Institute*, 43, 237–239.
- Applied Seismology Consultants (2014). *InSite Seismic Processor: user operation manual version 3.2*, Shrewsbury, UK: Author
- Brantut, N. (2018). Time-resolved tomography using acoustic emissions in the laboratory, and application to sandstone compactions. *Geophys. J. Int.*, 213: 2177-2192.
- Cole, D. M., & Dempsey, J. P. (2004). In situ sea ice experiments in McMurdo Sound: cyclic loading, fracture, and acoustic emissions. *Journal of cold regions engineering*, 18(4), 155-174.
- Cole, D. M., & Dempsey, J. P. (2006). Laboratory Observations of Acoustic Emissions from Antarctic First-Year Sea Ice Cores Under Cyclic Loading. In: *Proc. of the 18th Int. Conf. on Port and Ocean Eng. Under Arctic Conditions (POAC)*, Potsdam, USA
- Gold, L. W. (1960). The Cracking Activity in Ice During Creep.
- Gutenberg, B., and C. F. Richter (1944), Frequency of earthquakes in California,

Bulletin of the Seismological Society of America, 34(4), 185–188.

Hainzl, S. (2016). Rate-dependent incompleteness of earthquake catalogs. *Seismological Research Letters*. 87 (2A): 337-344.

Ishimoto, M., and K. Iida (1939), Observations sur les seismes enregistres par le microsismographe construit dernièrement (1), *Bull. Earthq. Res. Inst. Univ. Tokyo*, 17, 443–478.

Jiang

Kwiatek, G., K. Plenkers, M. Nakatani, Y. Yabe, G. Dresen, et al. (2010), Frequency-magnitude characteristics down to magnitude-4.4 for induced seismicity recorded at mponeng gold mine, south africa, *Bulletin of the Seismological Society of America*, 100(3), 1165–1173.

Langhorne, P. J., and T. G. Haskell. (1996). Acoustic emission during fatigue experiments on first year sea ice. *Cold regions science and technology* 24, no. 3: 237-250.

Langley, A.J., 1989. Acoustic emission from the Arctic ice sheet. *J. Acoust. Soc. Am.* 85 (2), 692-701

Lay, T., and T. C. Wallace (1995), *Modern global seismology*, vol. 58, Academic press.

Li, D., Du, F., 2016. Monitoring and evaluating the failure behavior of ice structure using the acoustic emission technique. *Cold Reg. Sci. Technol.* 129, 51–59.

Lishman, B., Marchenko, A., Shortt, M & Sammonds, P. (2019a). Acoustic emissions as a measure of damage in ice. In: *Proc. of the 25th Int. Conf. on Port and Ocean Eng. Under Arctic Conditions (POAC)*, Delft, Netherlands.

Lishman, B., Marchenko, A., Sammonds, P. and Murdza, A. (2019b). Acoustic emissions from in situ compression and indentation experiments on sea Ice

Lockner, D. (1993), The role of acoustic emission in the study of rock fracture, in *International Journal of Rock Mechanics and Mining Sciences & Geomechanics Abstracts*, vol. 30, pp. 883–899, Elsevier.

Main, I. (1996), Statistical physics, seismogenesis, and seismic hazard, *Reviews of Geophysics*, 34(4), 433–462.

Mair

Marchenko, Aleksey, Andrea Haase, Atle Jensen, Ben Lishman, Jean Rabault, Karl-Ulrich Evers, Mark Shortt, and Torsten Thiel (2019). Laboratory investigations of the bending rheology of floating saline ice, and physical mechanisms of wave damping, in the HSVA ice tank. (in review) arXiv preprint arXiv:1901.05333

Marchenko (2020)

Marzocchi, W., and L. Sandri (2003), A review and new insights on the estimation of the b-value and its uncertainty, *Annals of geophysics*

Michlmayr

Mogi, K. (1963), Magnitude-frequency relation for elastic shocks accompanying fractures of various materials and some related problems in earthquakes (2nd paper).

Rist, M. A. and S. A. F. Murrell. (1994). *Ice triaxial Deformation and Fracture*

Sammonds, P., P. Meredith, and I. Main (1992), Role of pore fluids in the generation of seismic precursors to shear fracture, *Nature*, 359 (6392), 228–230.

Sammonds, P. & Ohanaka, M. (1998). Evolution of microseismicity during frictional sliding. *Geophysical research letters*. vol. 25. no. 5: 699-702

Scourfield (2019). The influence of ice rubble on sea ice friction, PhD thesis, University College London

Scholz, C. (1968), The frequency-magnitude relation of microfracturing in rock and its relation to earthquakes, *Bulletin of the Seismological Society of America*, 58(1), 399–415.

Sinha (1982)

Sinha, (1985), Acoustic emission study on multi-year sea ice in an Arctic field laboratory. *J. Acoust. Emission*, 4 (2/3), pp. S290-S293

St Lawrence, William F., and David M. Cole (1982). Acoustic emissions from polycrystalline ice. No. CRREL-82-21. Cold Regions Research and Engineering Lab. Hanover NH.

Turcotte, D. L. (1997), *Fractals and chaos in geology and geophysics*, Cambridge university press.

Vogt, C., Laihem, K., Wiebusch, C. (2008). Speed of sound in bubble-free ice

Weiss, Jerome, and Jean-Robert Grasso (1997). "Acoustic emission in single crystals of ice." *The Journal of Physical Chemistry B* 101, no. 32: 6113-6117.

Xie, Y. and Farmer, D.M. (1994). Seismic-acoustic sensing of sea ice wave mechanical properties.